UDK 537.221:621.396.44
Original scientific article/Izvirni znanstveni članek

ISSN 1580-2949
Mater. Tehnol.

WIRELESS AND FLEXIBLE PIEZORESISTIVE PRESSURE SENSOR BASED ON MXENE-DECORATED ZIF-67/PAN HIERARCHICAL NANOCOMPOSITES INTEGRATED WITH PASSIVE RFID

FLEKSIBILNI BREZŽIČNI PIEZO-UPOROVNI TLAČNI SENZOR TEMELJEČ NA MXENE-DEKORIRANIH ZIF-67/PAN HIERARČNIH NANOKOMPOZITIH INTEGRIRANIH S PASIVNO RFID

Yage Wang[1*], Juan Gao[1], Ao Xu[2]

[1]School of Mechanics and Photoelectric Physics, Anhui University of Science and Technology, Huainan 232001, Anhui, China
[2]School of Mathematics and Big Data, Anhui University of Science and Technology, Huainan 232001, Anhui, China

Prejem rokopisa – received: 2025-12-21; sprejem za objavo – accepted for publication: 2026-04-22

doi:10.17222/mit.2025.1633

Existing flexible sensors often face inherent trade-offs between mechanical stability and signal linearity, further constrained by the 'wiring bottleneck' that restricts mobility. This study presents a robust, flexible piezoresistive sensor based on an MXene-decorated ZIF-67/polyacrylonitrile (PAN) nanocomposite, integrated with a passive ultra-high frequency (UHF) radio frequency identification (RFID) tag for battery-free wireless monitoring. By leveraging the high electrical conductivity of MXene ($Ti_3C_2T_x$), the hierarchical porous architecture of metal-organic framework ZIF-67, and the mechanical compliance of PAN nanofibers, the sensor achieves a synergistic sensing architecture. Spectroscopic and porosity analyses confirmed a strong chemical coordination between ZIF-67 nodes and the PAN fiber matrix. This interaction constructs a stable hierarchical scaffold that effectively prevents irreversible MXene restacking, reducing the relative standard deviation (RSD) of the response signal from > 80 % (pristine MXene) to ≈15 % at low pressures and < 2 % at higher pressures for the nanocomposite. The sensor demonstrated exceptional signal fidelity and superior durability, maintaining 92.4 % of its initial response after 3600 mechanical cycles and retaining 91.7 % of its electrical conductivity after 30 days of ambient exposure. Furthermore, wireless strain data acquisition was successfully achieved using an Impinj Speedway R420 reader with a read range of 10 cm. While shorter than logistics tags, this range is optimized for secure, near-field personal health monitoring, utilizing received signal strength indicator (RSSI) modulation. This work demonstrates the feasibility of integrating MOF-enhanced MXene composites with passive RFID technology, offering a scalable solution for reliable applications in wearable health devices and structural health monitoring (SHM).

Keywords: MXene, metal-organic framework, flexible pressure sensor, radio frequency identification

Pri obstoječih fleksibilnih senzorjih se pogosto soočamo z inherentnimi kompromisi med mehansko stabilnostjo in linearnostjo signala, ki še poslabšuje "ozko grlo v ožičenju", kar omejuje mobilnost. V članku avtorji predstavljajo študijo izdelave robustnega, fleksibilnega piezouporovnega senzorja, ki temelji na nanokompozitu ZIF-67/poliakrilonitril (PAN), dekoriranem z MXene, integriranem s pasivno oznako za radiofrekvenčno identifikacijo (RFID) z ultra visoko frekvenco (UHF) za brezžično spremljanje brez baterij. Z izkoriščanjem visoke električne prevodnosti MXene ($Ti_3C_2T_x$), hierarhične porozne arhitekture kovinsko-organskega ogrodja ZIF-67 in mehanske skladnosti nanovlaken PAN s senzorjem so avtorji dosegli sinergistično arhitekturo zaznavanja. Spektroskopske analize in analize poroznosti so potrdile močno kemijsko koordinacijo med vozlišči ZIF-67 in matriko vlaken PAN. Ta interakcija gradi stabilno hierarhično ogrodje, ki učinkovito preprečuje nepovratno ponovno zlaganje MXene in zmanjšuje relativni standardni odklon (RSD) odzivnega signala z >80 % (neokrnjen MXene) na č15 % pri nizkih tlakih in pod 2 % pri višjih tlakih za nanokompozit. Avtorji v članku poudarjajo, da so s senzorjem dosegli izjemno natančnost signala in vrhunsko vzdržljivost, saj je po 3600 mehanskih ciklih senzor ohranil 92,4 % svojega začetnega odziva in 91,7 % svoje električne prevodnosti po 30 dneh izpostavljenosti okolju. Poleg tega je bilo brezžično pridobivanje podatkov o deformacijah uspešno doseženo z uporabo bralnika Impinj Speedway R420 z dosegom branja 10 cm. Čeprav je ta doseg krajši od logističnih oznak, je ta doseg optimiziran za varno spremljanje osebnega zdravja v bližnjem polju z uporabo modulacije indikatorja jakosti prejetega signala (RSSI). S to raziskavo so avtorji dokazali izvedljivost integracije kompozitov MXene, izboljšanih z MOF, s pasivno tehnologijo RFID, kar ponuja prilagodljivo rešitev za zanesljive aplikacije v nosljivih zdravstvenih napravah in pri spremljanju strukturnega zdravja (SHM).

Ključne besede: Mxene, kovinsko-organski okvir, fleksibilen senzor tlaka, radiofrekvenčna identifikacija

1 INTRODUCTION

The wearable strain and pressure sensor market is projected to reach a multi-billion dollar value by 2030,[1] yet current solutions often struggle to balance longevity with efficient wireless operation. In the rapidly evolving field of flexible electronics, the integration of sensors with Radio Frequency Identification (RFID) technology has attracted considerable research interest.[2,3] While flexible sensors enable real-time monitoring of structural deformation and human motion, RFID technology provides a battery-free, wireless communication channel for automatic identification and data transmission.[4,5]

*Corresponding author's e-mail:
wyg_ge101@sina.com (Yage Wang)

The convergence of these technologies offers significant advantages for medical wearables[6,7] and infrastructure monitoring.[8] In medical applications, capturing human joint movements – which typically induce skin strains exceeding 30 % – and subtle physiological signals requires sensors that are both mechanically compliant and reliable.[9] However, existing MXene-based sensors are often prone to oxidative degradation and signal drift due to nanosheet restacking. Conversely, commercial strain gauges offer stability but lack the necessary flexibility for skin-mounting and typically require cumbersome wired connections. In structural health monitoring (SHM), detecting micro-cracks in harsh environments requires long-term stability, a challenge for wired sensors due to cable aging and deployment costs. Therefore, developing wireless sensors that combine reliable signal linearity, high flexibility (elongation at break >150 %), and environmental stability is critical.[10]

MXenes, a class of two-dimensional (2D) transition metal carbides and nitrides discovered in 2011,[11] are promising candidates for flexible sensors due to their metallic conductivity and hydrophilic nature.[12] However, primitive MXene films often suffer from limited resistance changes under strain and irreversible aggregation.[13] To address this, strategies such as interlayer intercalation have been employed to optimize conductivity.[14] Additionally, incorporating insulating or dielectric spacers can enhance the piezoresistive effect by creating stable tunneling pathways.

Despite progress, limitations remain. For instance, Fu et al.[15] developed an MXene/ZIF-67/PAN sensor with comparable sensitivity but relied on wired data acquisition. Similarly, while Luo et al.[16] achieved flexible integration using ZIF-derived MXene, the strain response range was limited (0.5–2 %), which is insufficient for monitoring large human motions. To address these limitations, this work presents a synergistic approach incorporating ZIF-67 – a metal-organic framework (MOF), similar to other 2D MOF sensing strategies,[17] with high porosity – and electrospun polyacrylonitrile (PAN) nanofibers to create a highly stable piezoresistive composite.[18,19]

Distinct from prior work, we integrate a passive RFID tag to enable wireless data acquisition, eliminating the need for on-board power supplies.[20,21] We propose a synergistic structural engineering strategy: (1) *in-situ* growth of ZIF-67 crystals on electrospun PAN nanofibers to serve as a 3D hierarchical scaffold for MXene anchoring. This architecture acts as a physical barrier to prevent the irreversible restacking of subsequently deposited MXene nanosheets, thereby preserving abundant active sites and tunneling pathways; (2) use of the flexible PAN nanofiber core to enhance mechanical durability (increasing elongation at break from 120 % to 180 %);[15] and (3) integration with a commercial UHF RFID platform (Impinj R420) to solve the 'wired bottleneck'. The resulting MZP-RFID sensor achieves a sensitivity of 0.021 kPa^{-1} with exceptional linearity and a secure near-field wireless read range of 10 cm, offering a robust solution for both wearable health and structural monitoring.

2 MATERIALS AND METHODS

2.1 Experimental reagents

The main reagents used in this study are listed in **Table 1**.

2.2 MXene@ZIF-67/PAN nanocomposite preparation

2.2.1 MXene ($Ti_3C_2T_x$) synthesis

MXene was synthesized via selective etching of the Al layer from the MAX phase precursor (Ti_3AlC_2) using a modified minimally intensive layer delamination (MILD) method. This milder etching approach was selected over traditional high-concentration HF etching because it provides safer operational conditions while minimizing structural defects, yielding larger and more pristine MXene flakes that are crucial for maintaining high electrical conductivity. Briefly, 4.5 g of LiF was dissolved in 55 mL of 9.5 M HCl to generate HF *in-situ*.[21] Then, 2.8 g of Ti_3AlC_2 powder was slowly added. The mixture was stirred at 35 °C for 24 h. The acidic product

Table 1: Main reagents

Main reagents	Grade	Manufacturer
Ti_3AlC_2	500 mesh	Jilin Yiyi Technology Co., Ltd.
HCl	37 %	Shanghai Aladdin Biochemical Technology Co., Ltd.
LiF	AR	Shanghai Aladdin Biochemical Technology Co., Ltd.
H_2SO_4	95.0–98.0 %	Beijing Chemical Reagent Factory
$Co(NO_3)_2{\cdot}6H_2O$	AR	Shanghai Aladdin Biochemical Technology Co., Ltd.
2-methylimidazole ($C_4H_6N_2$)	AR	Anhui Zesheng Technology Co., Ltd.
Methanol (CH_3OH)	AR	Anhui Zesheng Technology Co., Ltd.
Anhydrous ethanol (C_2H_5OH)	AR	Anhui Zesheng Technology Co., Ltd.
Silicone gel (PDMS)	/	SYLGARD
PAN ($(C_3H_3N)_n$)	average Mw 149000–151000	Shanghai Aladdin Biochemical Technology Co., Ltd.
N,N-dimethylformamide (C_3H_7NO)	AR	Shanghai Aladdin Biochemical Technology Co., Ltd.
H_2O	Ultra-pure	Laboratory-prepared (Milli-Q, 18.2 MÙ·cm)

was washed with deionized water and centrifuged (3600 min^{-1}) repeatedly until the supernatant pH reached approximately 7. The sediment was then dispersed in water, sonicated for 30 min under argon, and centrifuged to obtain a few-layer $Ti_3C_2T_x$ (f-MXene) supernatant with a concentration of ≈10 mg/mL.

2.2.2 $Co(NO_3)_2$/PAN fiber preparation

A precursor solution was formed by dissolving 0.27 g of $Co(NO_3)_2{\cdot}6H_2O$ in 5.5 mL of DMF, followed by an addition of 0.45 g of PAN. The mixture was stirred for 7 h at room temperature. The solution was electrospun using a voltage of 18 kV, a flow rate of 0.25 mL/h, and a tip-to-collector distance of 16 cm. The resulting nanofibers were dried at 65 °C for 14 h.[22]

2.2.3 ZIF-67/PAN fiber preparation

ZIF-67 crystals were grown *in-situ* on the PAN fibers following the method by Ginting et al.[23] The $Co(NO_3)_2$/PAN fibers were immersed in 45 mL of a methanolic solution containing 0.42 M 2-methylimidazole for 2.5 h. This allowed ZIF-67 to nucleate and grow on the fiber surface. The fibers were washed with methanol and deionized water, then vacuum-dried at 65 °C for 10 h.

2.2.4 MXene/ZIF-67/PAN (MZP) composite film formation

The MZP composite was fabricated via vacuum-assisted infiltration strategy. The ZIF-67/PAN fiber mat, possessing a highly porous non-woven structure, served as the 3D skeleton rather than a simple filtration membrane. The MXene suspension (prepared in 2.2.1) was permeated into this scaffold under controlled vacuum pressure.

Unlike traditional filtration that forms a dense filter cake on the surface, the abundant ZIF-67 nodes on the PAN fibers acted as anchoring sites, facilitating a uniform assembly of MXene nanosheets on individual fiber surfaces via electrostatic and coordination interactions. After the solution fully infiltrated the matrix, the vacuum was maintained briefly to strengthen the interfacial contact. The composite film was then dried at 65 °C for 7 h.

2.3 Flexible sensor assembly and RFID integration

The sensor with a sandwich structure was constructed. The MZP composite film (thickness of 25 ± 3 μm, area of 15 × 10 mm) served as the sensing layer, sandwiched between two protective layers of PDMS (each with a thickness of 500 μm). PDMS was specifically selected as the packaging material due to its excellent biocompatibility, chemical inertness, and mechanical flexibility, ensuring safe, comfortable, and prolonged epidermal contact for near-field personal health monitoring. Copper strip electrodes (width of 2 mm, spacing of 8 mm) were attached using conductive silver epoxy (MG Chemicals 8331S).

For wireless integration, a passive UHF RFID tag (Alien Technology, Higgs-9, 915 MHz) was coupled to the sensor. The piezoresistive sensor was connected in series with the tag's dipole antenna using conductive silver epoxy. To ensure a rigorous material comparison, the 'standard dipole' reference tag was also fabricated in the laboratory using the same conductive silver epoxy printing process on a PET substrate, rather than using a commercial etched-aluminum tag.

Data acquisition was performed using an Impinj Speedway R420 reader connected to a Laird S9028PCL antenna. To simulate the operational environment of handheld medical scanners and ensure near-field data security, the reader's transmission power was restricted to 20 dBm (unless otherwise specified). In this configuration, strain-induced resistance changes in the sensor modulate the impedance match between the antenna and the RFID chip, thereby altering the backscattered signal strength (RSSI).

2.4. Material characterization

The chemical structure and functional groups were analyzed using Fourier transform infrared spectroscopy (FTIR, Thermo Scientific Nicolet iS50) in the transmittance mode and X-ray photoelectron spectroscopy (XPS, Thermo Scientific K-Alpha) with Al Kα radiation. The specific surface area and pore size distribution were determined via N_2 adsorption-desorption isotherms at 77 K using a surface area analyzer (BET, Micromeritics ASAP 2020). Elemental composition and evolution were quantified using energy dispersive spectroscopy (EDS, Oxford Instruments). The crystalline phases were identified by X-ray diffraction (XRD, Rigaku SmartLab), and structural defects were probed using Raman spectroscopy (Horiba LabRAM, 532 nm laser).

2.5 Performance testing

Electromechanical properties were tested using a Keithley 2400 source meter coupled with a universal testing machine (Instron 5965) or a linear actuator (Thorlabs Z825B). Pressure sensitivity (S) was calculated from the slope of the relative current change versus applied pressure curves, as defined in Equation (1):

$$S = \frac{\mathrm{d}\left(\frac{I}{I_0}\right)}{\mathrm{d}P} \tag{1}$$

where I is the real-time measured current, I_0 is the initial current, and P is the applied pressure. The term I/I_0 represents the normalized current response. Consequently, S is defined as the slope of the normalized current curve with respect to pressure. Since the measurements were conducted under a constant voltage supply (V), the current variation is intrinsically linked to the resistance change by Ohm's law, making $\mathrm{d}(I/I_0)$ an effective indicator of the piezoresistive performance.

3 RESULTS AND DISCUSSION

3.1 Chemical and structural evolution of the composite

Given that the dense stacking of 2D nanosheets often obscures the internal architecture in morphological observations, we employed a comprehensive suite of spectroscopic and porosity analyses to rigorously verify the *in-situ* growth and structural integration of the MZP nanocomposite.

Figure 1 presents the chemical and structural evolution of the material from pristine MXene to the final MZP composite. **Figure 1a** displays the FTIR spectra. The MZP composite inherits the characteristic nitrile (C ≡ N) peak at 2243 cm^{-1} from the PAN nanofiber matrix. Crucially, a distinct absorption band emerges at 425 cm^{-1}, corresponding to the Co-N stretching vibration. This provides direct evidence of the chemical coordination between the ZIF-67 metal centers and the nitrogenous ligands on the fiber surface, rather than a mere physical mixture. Additionally, the broad -OH stretching band (≈3430 cm^{-1}) observed in pristine MXene is significantly attenuated in the MZP spectrum, suggesting an effective coverage of MXene surface terminations by the ZIF-67 layer.

The impact of this integration on the pore structure was quantified via N_2 adsorption-desorption isotherms (**Figure 1b**). Pristine MXene exhibits a non-porous Type II isotherm with a low specific surface area (S_{BET} ≈ 28 m^2 g^{-1}), confirming its tendency to restack. The introduction of PAN fibers (MXene/PAN) only moderately increases the surface area to ≈75 m^2 g^{-1}. In sharp contrast, the MZP composite displays a Type IV isotherm with a pronounced hysteresis loop ($P/P_0 > 0.45$), characteristic of a hierarchical porous structure combining the intrinsic microporosity of ZIF-67 and the mesoporosity of the fibrous network. Furthermore, the pore size distribution confirms the coexistence of micropores (< 2 nm, originating from the intrinsic ZIF-67 cavities) and mesopores (predominantly 2–50 nm, arising from the interstitial spaces between the nanofiber scaffold and MXene sheets). The S_{BET} dramatically increases to 585 m^2 g^{-1}. This exceptionally high surface area provides compelling evidence that the MXene nanosheets have successfully infiltrated the fiber mat and wrapped around the ZIF-67/PAN fibers, rather than merely accumulating as a dense layer on the surface. This structural configuration confirms the efficacy of the vacuum-assisted infiltration method: the ZIF-67 nodes act as effective dielectric 'spacers' that prevent the irreversible restacking of MXene sheets, maintaining the open hierarchical porosity essential for high sensitivity.

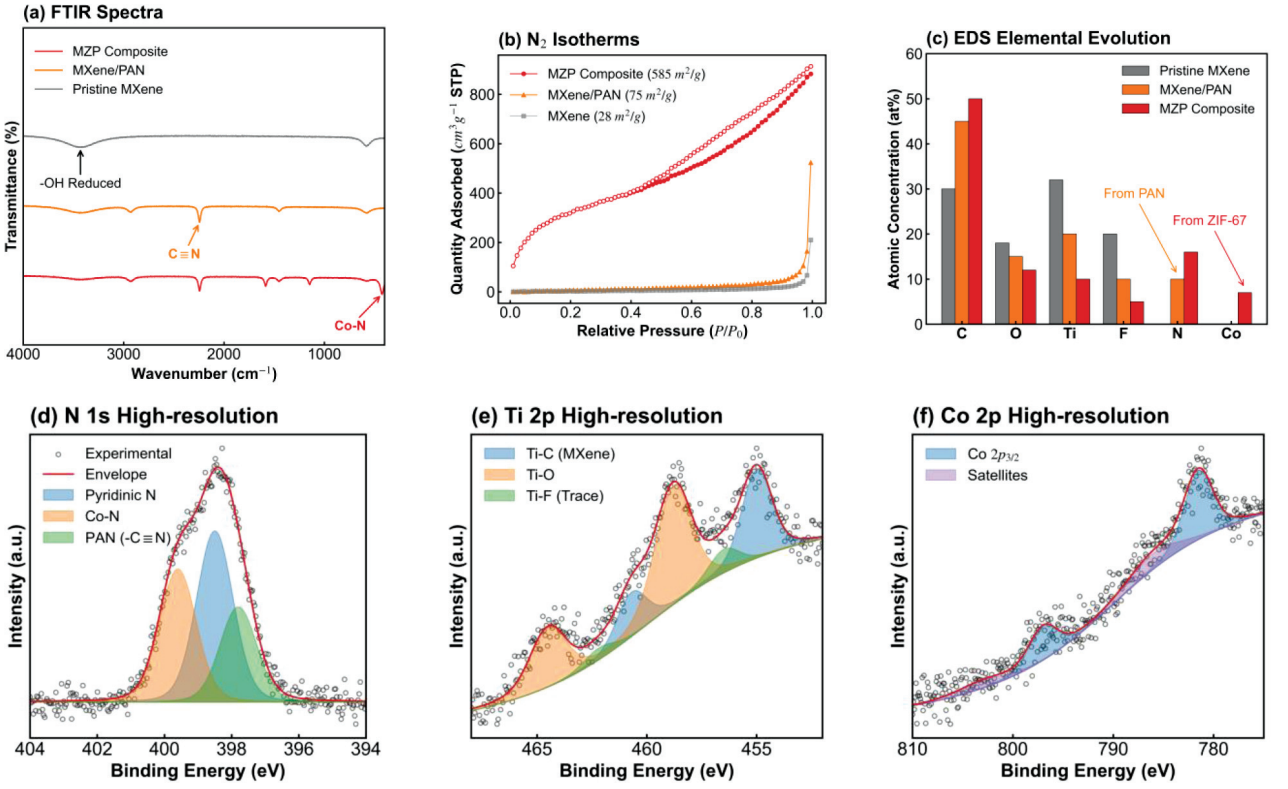

Figure 1: Chemical and structural evolution of the nanocomposites: a) FTIR spectra showing the emergence of the Co-N stretching vibration at 425 cm^{-1}, indicating coordination between ZIF-67 and the PAN matrix; b) N_2 adsorption-desorption isotherms. The MZP composite exhibits a Type IV isotherm with a specific surface area of 585 m^2 g^{-1}, significantly higher than pristine MXene; c) EDS elemental evolution confirming the uniform loading of Co and N elements; d–f) high-resolution XPS spectra of d) N 1s, e) Ti 2p, and f) Co 2p, verifying the chemical anchoring of ZIF-67 crystals on the MXene/PAN framework

The elemental evolution was further tracked by EDS (**Figure 1c**). Pristine MXene shows no nitrogen or cobalt signals. In the MXene/PAN intermediate, nitrogen appears (≈10.0 at.%) due to the PAN (C_3H_3N) backbone. In the final MZP composite, the nitrogen content rises to ≈16.0 at.%, and cobalt emerges at ≈7.0 at.%, confirming the successful loading of ZIF-67. Concurrently, the relative atomic concentration of surface fluorine decreases from 20.0 % to 5.0 %, further validating the uniform encapsulation of the MXene sheets.

To gain deeper insight into the interfacial bonding, X-ray photoelectron spectroscopy (XPS) was performed. The high-resolution N 1s spectrum (**Figure 1d**) reveals a deconvoluted peak at 399.6 eV. According to previous studies on ZIF-67 derivatives,[15,23] this binding energy is characteristic of the Co-N coordination bond, distinguishing it from the pyridinic-N (398.5 eV) and the nitrile-N (397.8 eV) signals originating from the PAN backbone. This finding is further corroborated by the Co 2p spectrum (**Figure 1f**), where the binding energy of Co $2p_{3/2}$ at 781.5 eV indicates the oxidized Co(II) state bonded to nitrogen. Concurrently, the Ti 2p spectrum (**Figure 1e**) shows a suppression of the Ti-F signal compared to pristine MXene literature values, indicating the effective coverage of the MXene surface. The coexistence of these specific signals confirms the strong chemical anchoring of ZIF-67 nodes onto the nanofiber framework, ruling out simple physical adsorption.

The crystalline phase evolution was monitored by XRD (**Figure 2**). The shift of the MXene (002) peak from 6.8° to 5.8° confirms the expansion of interlayer spacing, attributed to the intercalation of PAN chains and ZIF-67 nucleation. Raman spectroscopy (**Figure 3**) reveals a reduction in the I_D/I_G ratio for the MZP composite, suggesting that ZIF-67 nodes preferentially nucleate

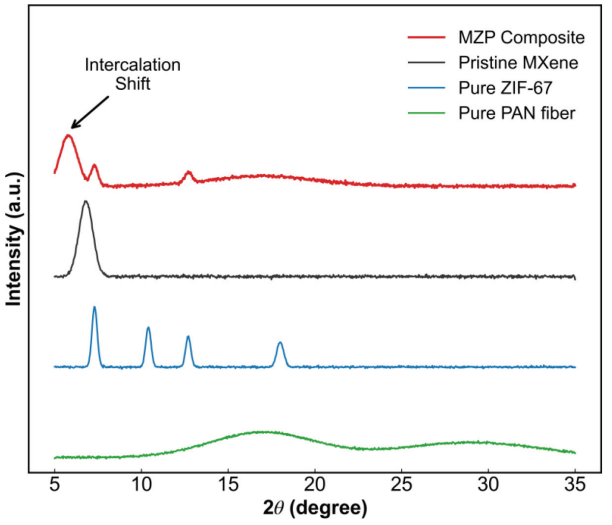

Figure 2: X-ray diffraction (XRD) patterns of pure PAN fiber, pure ZIF-67, pristine MXene, and the MZP composite. The shift of the MXene (002) peak from 6.8° to 5.8° in the MZP spectrum confirms the expansion of interlayer spacing due to the *in-situ* intercalation of ZIF-67 and PAN chains.

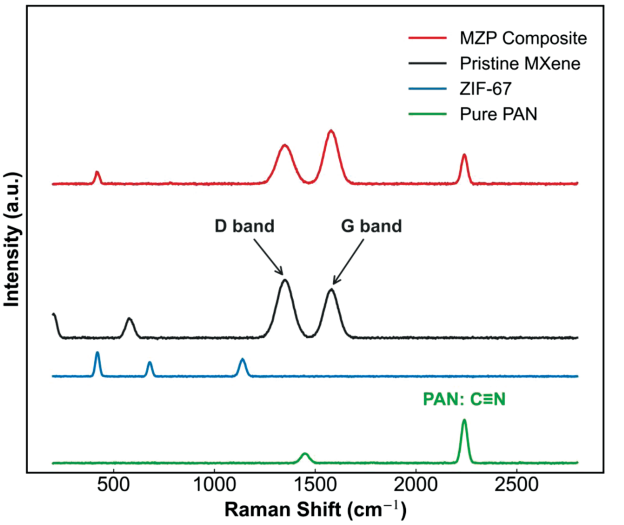

Figure 3: Raman spectra comparison. The MZP composite displays characteristic D and G bands alongside ZIF-67 and PAN fingerprints. The variation in the I_D/I_G ratio suggests that ZIF-67 nucleation preferentially occurs at defect sites, effectively stabilizing the MXene nanosheets.

at the defect sites of MXene nanosheets, effectively 'repairing' the conductive network.

Furthermore, electron spin resonance (ESR) was employed to probe the defect states and oxidation resistance (**Figure 4**). Pristine MXene displays a sharp symmetric signal at g ≈ 1.99 (322 mT), characteristic of Ti^{3+} paramagnetic centers. In the MZP composite, this signal is preserved but broadened due to the superposition with the Co^{2+} signal from ZIF-67 and the modification of the spin environment. Crucially, the persistence of the Ti^{3+} signal confirms that the MXene lattice remains protected from severe oxidation during the *in-situ* growth process, validating the efficacy of the ZIF-67/PAN encapsulation strategy. To further corroborate the practical environmental stability, the electrical resistance of the sensors was monitored under ambient conditions (temperature: ≈25 °C, relative humidity: ≈40–50 %) for 30 d (**Figure 4b**). The pristine MXene sensor exhibited a drastic increase in resistance ($R/R_0 > 5.0$), indicating severe degradation of the conductive $Ti_3C_2T_x$ network into insulating titanium oxides. Conversely, the MZP sensor demonstrated remarkable stability. As shown in the inset of **Figure 4b**, the resistance of the MZP composite increased only marginally ($R/R_0 \approx 1.09$) over the entire testing period. This corresponds to a conductivity retention of 91.7 %, confirming that the dense ZIF-67/PAN shell effectively shields the inner MXene nanosheets from moisture and oxygen, thereby resolving the long-standing instability issue of MXene-based electronics.

3.2. Electromechanical performance

The electromechanical performance of the sensor was evaluated in comparison with control groups (**Figure 5**).

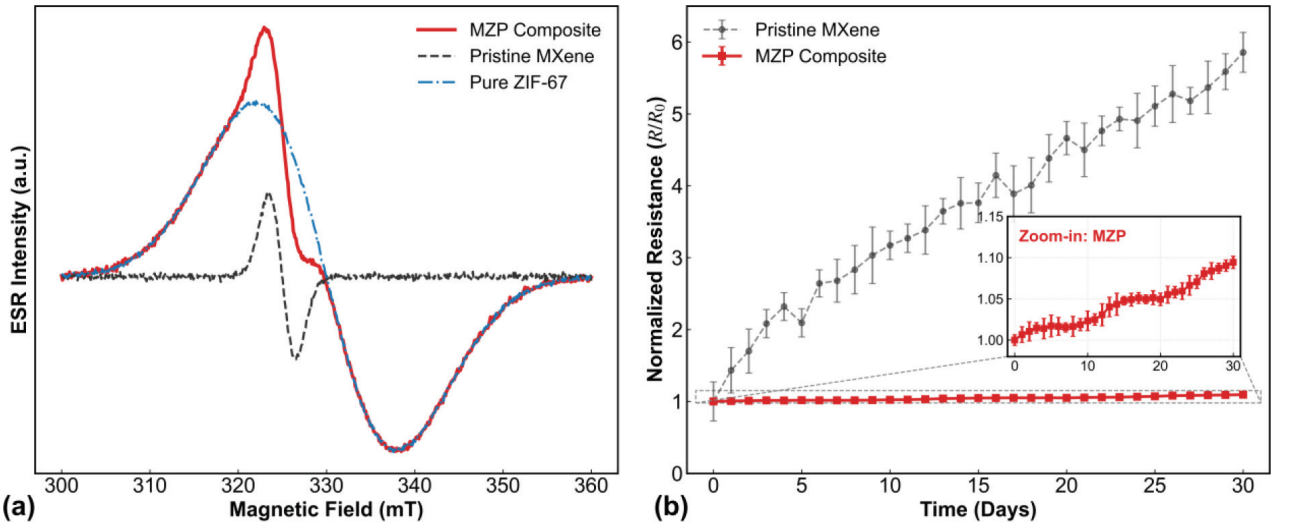

Figure 4: Analysis of oxidation resistance: a) electron spin resonance (ESR) spectra. The persistence of the Ti^{3+} signal (g ≈ 1.99) in the MZP composite confirms that the MXene lattice is chemically protected; b) long-term environmental stability test showing the normalized resistance change (R/R_0) over 30 d in ambient air. The pristine MXene sensor (gray dashed line) exhibits a sharp resistance increase due to oxidation. In contrast, the MZP sensor (red solid line) maintains exceptional stability. The inset (zoom-in view) reveals that the MZP sensor experiences only a marginal resistance drift ($R/R_0 \approx 1.09$) after 30 d, corresponding to a 91.7 % retention of initial electrical conductivity.

Figure 5a compares the pressure sensitivity of pure MXene, MXene/PAN, and the MZP composite. The pure MXene sensor exhibits low sensitivity ($S \approx 0.005$ kPa^{-1}) and early saturation, attributed to the dense stacking of nanosheets which limits the effective contact area variation. The MXene/PAN sensor shows improved linearity due to the fibrous network but remains at a moderate sensitivity level (0.012 kPa^{-1}). In contrast, the MZP sensor achieves the highest sensitivity of 0.021 kPa^{-1}. Crucially, while this absolute value is moderate compared to sensors utilizing fragile high-aspect-ratio microstructures,[24,25] it represents a strategic trade-off to secure exceptional signal fidelity and linearity ($R^2 > 0.99$). The rigorous anchoring of MXene nanosheets onto the ZIF-67-decorated PAN scaffold prevents random nanosheet sliding, thereby eliminating signal spikes and ensuring that the electrical response faithfully follows the mechanical stimulus without overshooting. This enhancement is attributed to the synergistic effect: ZIF-67 nodes act as robust dielectric 'spacers' that regulate the initial contact resistance and maintain stable tunneling pathways, while the PAN network provides elastic recoverability. This structural configuration results in a distinct, mechanism-dependent response: under compressive pressure, the ZIF-67 spacers are compressed to shorten the tunneling distance, leading to a resistance drop (positive current response, **Figure 5a**); conversely, under tensile strain (as discussed in Section 3.3), the network stretches and expands, increasing resistance (negative current response).

Figure 5b illustrates the hysteresis loop of the MZP sensor. Thanks to the elastic support of PAN nanofibers, the sensor exhibits negligible hysteresis during the loading-unloading cycle, distinguishing it from the viscoelastic behavior typically seen in pure polymer-based sensors.

Finally, the long-term mechanical durability of the sensor was evaluated to ensure reliability for practical

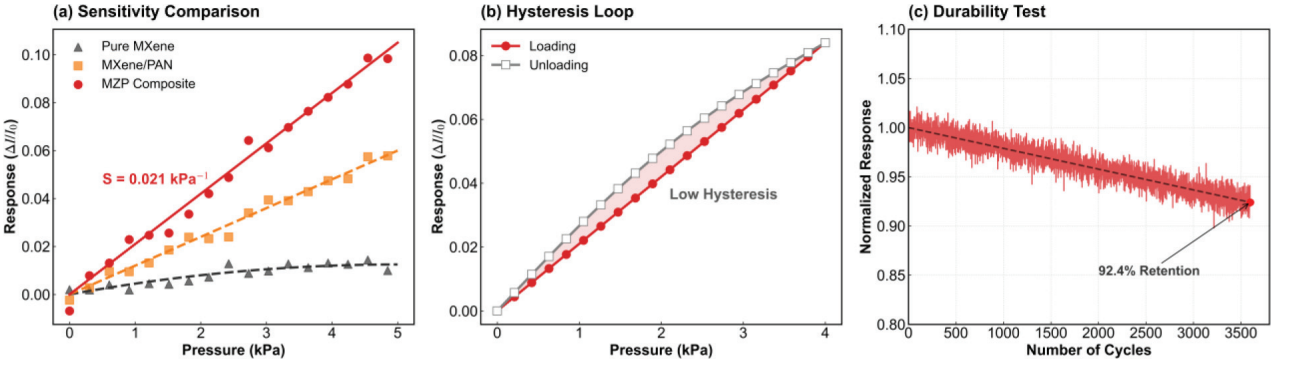

Figure 5: Electromechanical performance of the sensors: a) pressure sensitivity comparison among pure MXene, MXene/PAN, and MZP sensors. The MZP sensor achieves a linear sensitivity of 0.021 kPa^{-1} ($R^2 > 0.99$) without early saturation; b) hysteresis loop of the MZP sensor during a loading-unloading cycle, demonstrating excellent elastic recovery attributed to the PAN nanofiber substrate; c) durability test of the MZP sensor under 3600 loading-unloading cycles, showing a signal retention of 92.4 %, validating the structural stability of the nanocomposite.

applications. As shown in **Figure 5c**, the sensor was subjected to 3600 continuous loading-unloading cycles at a frequency of 1 Hz. The normalized electrical response exhibits exceptional stability with negligible baseline drift. Even after 3600 cycles, the sensor maintained 92.4 % of its initial response amplitude. This outstanding fatigue resistance is attributed to the hierarchical MZP architecture, where the ZIF-67 nodes effectively prevent the sliding and irreversible stacking of MXene nanosheets, while the elastic PAN nanofiber core ensures reversible deformation.

Stability is a critical parameter for practical applications. **Figure 6** compares the sensitivity error (relative standard deviation, RSD) of the pristine MXene sensor versus the MZP sensor. The pristine MXene sensor suffers from significant signal fluctuations (RSD > 80 %) in the low-pressure range (< 100 Pa) due to unstable contact points. Conversely, the MZP sensor demonstrates remarkable stability. Even at a subtle pressure of 50 Pa, it maintains an average RSD of ≈15 % (a drastic improvement compared to the control group), which further drops to < 2 % at higher pressures. This superior signal-to-noise ratio validates the role of the ZIF-67-decorated PAN scaffold in stabilizing a conductive percolation network under dynamic deformation.

3.3. Real-time sensing performance and wireless feasibility

To evaluate the sensor's intrinsic electromechanical response without the bandwidth limitations imposed by commercial RFID communication protocols, we first conducted real-time monitoring using a high-speed wired connection (Keithley 2400). While the sensor material exhibits a rapid response time, standard UHF RFID readers (like Impinj R420) typically offer discrete sampling rates (< 50 Hz effective data rate per tag) limited by anti-collision algorithms, challenging the reconstruction of high-fidelity dynamic waveforms. Therefore, wired measurements were employed to rigorously characterize the signal fidelity and transient response. **Figure 7a** compares the transient response of the pure MXene and MZP sensors. The pure MXene sensor shows a sluggish recovery (trailing tail) due to the irreversible sliding of nanosheets. In contrast, the MZP sensor exhibits a rapid response time of 40 ms and a recovery time of 30 ms, enabling the detection of high-frequency dynamic signals without signal hysteresis.

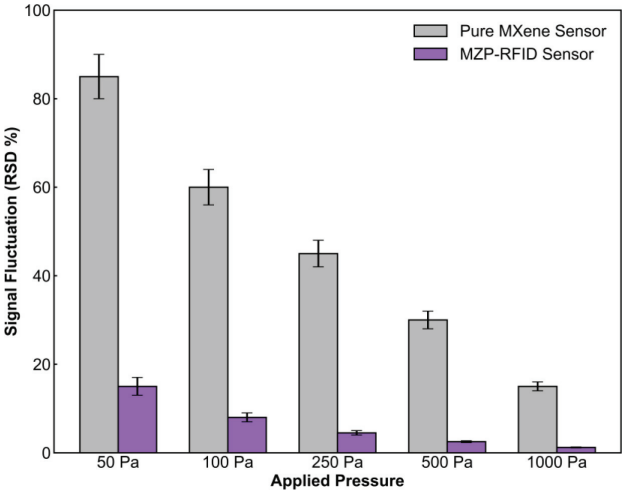

Figure 6: Signal stability analysis. Comparison of the signal stability (RSD) between the pure MXene sensor and the MZP-RFID sensor across different pressure regimes. The MZP sensor maintains an RSD < 2 % at higher pressures and < 15 % at 50 Pa, significantly outperforming the pristine MXene sensor (> 80 % error at low pressure) by stabilizing the conductive percolation network.

As shown in **Figure 7b** (measured via a high-precision wired source meter), the sensor successfully captured the radial artery pulse waveform. It is worth noting that while the absolute sensitivity (0.021 kPa^{-1}) is moderate compared to sensors designed with unstable microstructures, the MZP sensor excels in signal fidelity. Specifically, the ZIF-67-decorated PAN scaffold creates a robust conductive percolation network with an ultra-low electrical noise floor. Consequently, even though the subtle pulse pressure (≈0.5 kPa) induces a relatively small current change, the signal-to-noise ratio (SNR) remains exceptionally high. This allows distinct physiological features, such as the P-wave (percussion wave, representing early systolic ejection) and D-wave (dicrotic wave, reflecting aortic valve closure and peripheral vascular resistance) to be clearly resolved from the background. Successfully distinguishing these subtle physiological phases avoids baseline fluctuations often observed in ultra-sensitive but structurally unstable devices, thereby demonstrating the sensor's high signal fidelity for clinical applications.

Furthermore, the sensor was attached to the outer elbow joint to monitor large-scale human motions (**Figure 7c**). In this configuration, elbow flexion (bending angle of approximately 90°, corresponding to an estimated applied strain of ≈30–40 %) induces significant tensile strain on the sensor. Consistent with the piezoresistive mechanism of the conductive network, the stretching of the PAN scaffold increases the tunneling distance between MXene nanosheets, resulting in a rise in resistance. Accordingly, the monitored current exhibits a distinct and repeatable drop (from a baseline of ≈180 μA to ≈30 μA) when the arm is bent (the bent state) and rapidly recovers to the initial level upon extension (the relaxed state). This stable negative response under large strains further verifies the mechanical robustness of the hierarchical nanocomposite, which maintains electrical continuity even under significant deformation.

Building on these sensing characteristics, we further demonstrated the feasibility of wireless data transmission by integrating the sensor with a passive RFID tag. **Figure 8** compares the received signal strength indicator (RSSI) values of RFID tags fabricated with different materials. It is important to note that the 'standard dipole'

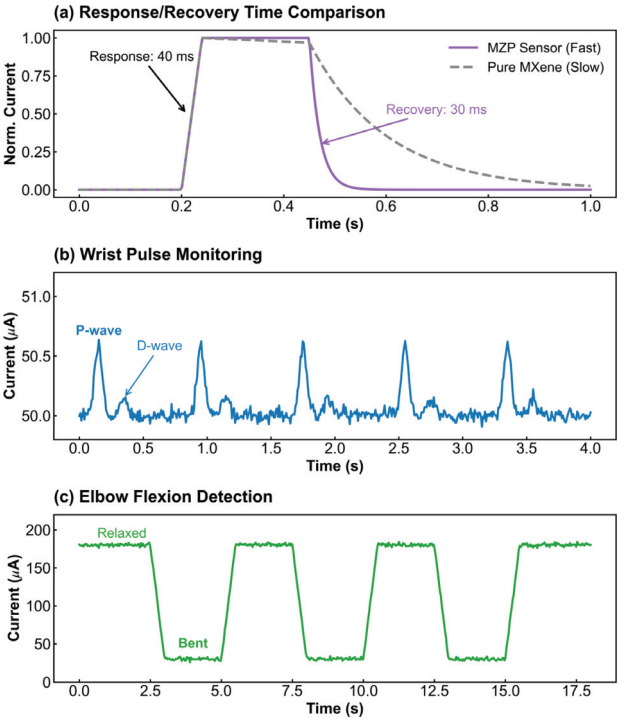

Figure 7: Real-time sensing performance: a) transient response and recovery time comparison. The MZP sensor exhibits a fast response of 40 ms; b) monitoring of the radial artery pulse waveform. Despite the moderate sensitivity, the high signal-to-noise ratio (SNR) allows clear distinction between P-wave and D-wave features; c) current response to large-scale elbow flexion motions monitored at the outer elbow. The distinct current drop during bending corresponds to the resistance increase caused by tensile strain, demonstrating excellent mechanical stability and repeatability.

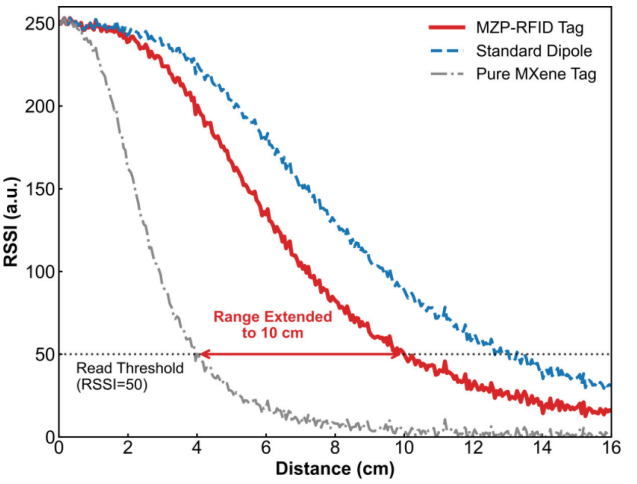

Figure 8: Wireless communication performance. Comparison of received signal strength indicator (RSSI) decay versus distance under a low-power setting (20 dBm). The reference dipole (fabricated via silver epoxy printing) exhibits a baseline range of ≈14 cm. The optimized MZP-RFID tag (red solid line) maintains a readable signal (RSSI > 50) up to 10 cm, whereas the tag based on pure MXene (gray dashed line) becomes unreadable beyond ≈4 cm. This extension is attributed to the improved impedance matching provided by the dielectric ZIF-67/PAN composite.

(blue dashed line) represents a reference tag printed with conductive silver epoxy to ensure material consistency with the sensor tags, rather than a highly conductive industrial aluminum tag.

Under a secure, low-power interrogation condition (20 dBm), the standard silver-epoxy tag shows a read range of ≈14 cm. The tag based on pure MXene shows a rapid signal decay, becoming unreadable beyond 4 cm due to severe impedance mismatch. In contrast, the optimized MZP-RFID tag exhibits an extended effective read range of 10 cm (threshold RSSI > 50). While this range is naturally shorter than that of logistics tags operating at full power (> 30 dBm), the observed 10 cm range is deliberately optimized for body area networks (BAN). It effectively restricts data transmission to a secure 'personal zone,' providing a physical security layer that prevents unauthorized remote interception (eavesdropping) of sensitive physiological data while remaining accessible to handheld readers. This improvement arises from the tunable impedance provided by the ZIF-67-decorated PAN scaffold. The dielectric ZIF-67 nodes and insulating PAN matrix modulate the complex impedance of the sensor. Instead of pursuing perfect resonance for maximum range, an antenna is engineered to operate on the steep slope of the impedance matching curve. Crucially, the high wireless responsiveness is achieved by engineering the antenna's operating point to sit on the steep slope of the impedance matching curve, rather than at the flat peak of perfect resonance. In this configuration, the MZP sensor acts as a variable load that maintains the system in a high-sensitivity detuning region.

According to the power transfer theory, the backscattered power depends non-linearly on the power transmission coefficient (τ) between the chip and the antenna. Even a minute resistance variation (e.g., ≈1 % induced by subtle pulse pressure) causes the impedance state to slide down this steep resonance slope, triggering a disproportionately large drop in τ and a significant, detectable shift in RSSI. This 'slope-amplified' mechanism effectively bypasses the limitation of the sensor's moderate intrinsic piezoresistive sensitivity (0.021 kPa^{-1}), allowing for reliable wireless event detection without requiring ultra-high material sensitivity. Specifically, the highly stable dielectric ZIF-67 nodes contribute to maintaining this steep slope state by providing a stable baseline capacitance and regulating the initial impedance matching point, which directly translates minute mechanical deformations into substantial, amplified wireless signal variations.

4 CONCLUSIONS

This work successfully demonstrates a wireless, flexible piezoresistive sensor based on an MXene@ZIF-67/PAN nanocomposite.

Material Synergy: The effective anchoring of MXene on the ZIF-67-modified PAN nanofiber framework was confirmed via XPS and BET analyses, which revealed

stable Co-N coordination and a high specific surface area (585 $m^2\ g^{-1}$). This hierarchical structure effectively mitigated oxidative degradation (conductivity retained at 91.7 % after 30 d) and improved mechanical flexibility.

Sensing Performance: The sensor delivers a highly linear response with a sensitivity of 0.021 kPa^{-1}. While the sensitivity magnitude is moderate, the sensor achieves exceptional linearity ($R^2 > 0.99$) and signal stability (RSD < 2 %), overcoming the noise and hysteresis issues common in pristine MXene sensors.

Wireless Capability: By integrating the sensor with a passive RFID tag, we achieved battery-free wireless monitoring with a 10 cm effective range (under low-power handheld simulation). The system leverages the 'slope-amplified' detuning mechanism, where the ZIF-67 integration optimizes the impedance operating point to ensure that micro-deformations induce significant RSSI shifts, enabling high-fidelity wireless sensing.

This scalable approach addresses the 'wiring bottleneck' in wearable electronics and offers a promising pathway for the development of IoT-enabled health and infrastructure monitoring systems. While the optimized 10 cm read range successfully establishes a secure data transmission zone for body area networks (BAN), it practically imposes spatial restrictions on user mobility and requires close reader proximity during dynamic body movements. Future work will focus on antenna miniaturization and layout optimization to address these mobility limitations and extend the wireless read range to > 50 cm, alongside developing custom high-sampling-rate interrogation algorithms to fully exploit the sensor's fast response (40 ms) for wireless high-fidelity pulse waveform monitoring.

Acknowledgment

This work was supported by the Natural Science Research Project of Anhui Educational Committee (Grant No. KJ2021A0451) and the Open Research Fund of Anhui Province Engineering Laboratory for Big Data Analysis and Early Warning Technology of Coal Mine Safety (Grant No. CSBD2022-ZD02).

5 REFERENCES

[1] S. Wang, H. Zhai, Q. Zhang, X. Hu, Y. Li, X. Xiong, L. Wu, Trends in flexible sensing technology in smart wearable mechanisms–materials–applications, Nanomaterials, 15 (**2025**) 4, 298, doi:10.3390/nano15040298

[2] L. Yu, B. Liu, Y. Wang, F. Yu, J. Ma, Recent progress on MXene-derived material and its application in energy and environment, J. Power Sources, 490 (**2021**), 229250, doi:10.1016/j.jpowsour.2020.229250

[3] R. Singh, E. Singh, H. S. Nalwa, Inkjet printed nanomaterial based flexible radio frequency identification (RFID) tag sensors for the internet of nano things, RSC Adv., 7 (**2017**) 77, 48597–48630, doi:10.1039/c7ra07191d

[4] L. Zhang, J. Bi, Z. Zhao, Y. Wang, D. Mu, B. Wu, Sulfur@Self-Assembly 3D MXene hybrid cathode material for lithium-sulfur batteries, Electrochim. Acta, 370 (**2021**), 137759, doi:10.1016/j.electacta.2021.137759

[5] G. Yang, L. Xie, M. Mantysalo, X. Zhou, Z. Pang, L. D. Xu, A health-IoT platform based on the integration of intelligent packaging, unobtrusive bio-sensor and intelligent medicine box, IEEE Trans. Ind. Inform., 10 (**2014**) 4, 2180–2191, doi:10.1109/TII.2014.2307795

[6] C. I. Idumah, Emerging advancements in MXene polysaccharide bionanoarchitectures and biomedical applications, Int. J. Polym. Mater. Polym. Biomater., 72 (**2023**) 17, 1375–1396, doi:10.1080/00914037.2022.2098297

[7] K. Y. P. S. Avelino, L. S. Oliveira, N. Lucena-Silva, C. A. S. Andrade, M. D. L. Oliveira, Flexible sensor based on conducting polymer and gold nanoparticles for electrochemical screening of HPV families in cervical specimens, Talanta, 226 (**2021**), 122118, doi:10.1016/j.talanta.2021.122118

[8] Y. Wang, Y. Hui, X. Chen, K. Wen, S. Cheng, Q. Song, Multifunctional MXene/carbon nanotubes coated glass fiber sensors for *in-situ* monitoring of curing process and structural health of polymeric composites, Chem. Eng. J., 497 (**2024**) 1, 154386, doi:10.1016/j.cej.2024.154386

[9] Q. Shu, Z. Xu, S. Liu, J. Wu, H. Deng, X. Gong, S. Xuan, Magnetic flexible sensor with tension and bending discriminating detection, Chem. Eng. J., 433 (**2022**) 1, 134424, doi:10.1016/j.cej.2021.134424

[10] Y. Wang, Y. Xia, P. Xiang, Y. Dai, Y. Gao, H. Xu, J. Yu, G. Gao, K. Chen, Protein-assisted freeze-tolerant hydrogel with switchable performance toward customizable flexible sensor, Chem. Eng. J., 428 (**2022**), 131171, doi:10.1016/j.cej.2021.131171

[11] M. Naguib, J. Come, B. Dyatkin, V. Presser, P.-L. Taberna, P. Simon, Y. Gogotsi, MXene: a promising transition metal carbide anode for lithium-ion batteries, Electrochem. Commun., 16 (**2012**) 1, 61–64, doi:10.1016/j.elecom.2012.01.002

[12] B. J. Tok, Z. Bao, Recent advances in flexible and stretchable electronics, sensors and power sources, Sci. China Chem., 55 (**2012**) 5, 718–725, doi:10.1007/s11426-012-4601-5

[13] Y.-M. Shi, X. Zhang, L. Mei, K. Hu, L.-Q. Chao, X.-M. Li, M.-S. Miao, 2D Accordion-like MXene nanosheets as a sensitive electrode material for Baicalin sensing, Electroanalysis, 33 (**2021**) 5, 1308–1314, doi:10.1002/elan.202060535

[14] P. Xu, H. Xiao, X. Liang, T. Zhang, F. Zhang, C. Liu, B. Lang, Q. Gao, A MXene-based EDA-$Ti_3C_2T_x$ intercalation compound with expanded interlayer spacing as high performance supercapacitor electrode material, Carbon, 173 (**2021**), 135–144, doi:10.1016/j.carbon.2020.11.010

[15] X. Fu, J. Li, D. Li, L. Zhao, Z. Yuan, V. Shulga, W. Han, L. Wang, MXene/ZIF-67/PAN nanofiber film for ultra-sensitive pressure sensors, ACS Appl. Mater. Interfaces, 14 (**2022**) 10, 12367–12374, doi:10.1021/acsami.1c24655

[16] S. Luo, Z. Wu, J. Zhao, Z. Luo, Q. Qiu, Z. Li, H. Wu, G. Xing, C. Wu, ZIF-67 derivative decorated MXene for a highly integrated flexible self-powered photodetector, ACS Appl. Mater. Interfaces, 14 (**2022**) 17, 19725–19735, doi:10.1021/acsami.2c03148

[17] S. E. A. Elashery, N. F. Attia, H. Oh, Design and fabrication of novel flexible sensor based on 2D Ni-MOF nanosheets as a preliminary step toward wearable sensor for onsite Ni(II) ions detection in biological and environmental samples, Anal. Chim. Acta, 1197 (**2022**), 39518, doi:10.1016/j.aca.2022.339518

[18] M. Wang, Y. Cheng, H. Zhang, F. Cheng, Y. Wang, T. Huang, Z. Wei, Y. Zhang, B. Ge, Y. Ma, Y. Yue, Y. Gao, Nature-inspired interconnected macro/meso/micro-porous MXene electrode, Adv. Funct. Mater., 33 (**2023**) 12, 1–11, doi:10.1002/adfm.202211199

[19] B. Li, B. Zhou, Z. Qu, Q. Song, Z. Jiang, Theoretical study on Fe_2C MXene as electrode material for secondary battery, Chem. Phys., 548 (**2021**), 111223, doi:10.1016/j.chemphys.2021.111223

[20] W. Yang, X. Cheng, Z. Guo, Q. Sun, J. Wang, C. Wang, Design, fabrication and applications of flexible RFID antennas based on printed

electronic materials and technologies, J. Mater. Chem. C, 11 (**2023**), 406–425, doi:10.1039/D2TC03736J

[21] B. Gurzęda, N. Boulanger, A. Nordenström, C. Dejoie, A. V. Talyzin, Pristine MXene: *in situ* XRD study of MAX phase etching with HCl+ LiF solution, Adv. Sci., 11 (**2024**), 2408448, doi:10.1002/advs.202408448

[22] C. H. Yang, Y. C. Hsiao, L. Y. Lin, Novel *in situ* synthesis of free-standing carbonized ZIF67/polymer nanofiber electrodes for supercapacitors via electrospinning and pyrolysis techniques, ACS Appl. Mater. Interfaces, 13 (**2021**), 41637–41648, doi:10.1021/acsami.1c10985

[23] R. T. Ginting, H. Abdullah, D. A. Barus, V. Fauzia, Extremely high-efficiency solar steam generation, robust and scalable photothermal evaporator based on ZIF-67@MXene/rGO decorated rock wool, J. Mater. Chem. A, 11 (**2023**) 10, 5296–5308, doi:10.1039/d2ta09778h

[24] L. Zhao, S. Yu, J. Li, Z. Song, M. Wu, X. Wang, X. Wang, Biomimetic-inspired highly sensitive flexible capacitive pressure sensor with high-aspect-ratio microstructures, Curr. Appl. Phys., 31 (**2021**), 29–37, doi:10.1016/j.cap.2021.07.014

[25] M. Wang, L. Mu, H. Zhang, S. Ma, Y. Liang, L. Ren, Flexible strain sensor with ridge-like microstructures for wearable applications, Polym. Adv. Technol., 33 (**2022**) 1, 96–103, doi:10.1002/pat.5493